metrology

Article

A Lightweight UAV-Mounted Metrology System for Standards-Aligned Metric Crack Width Measurement in Reinforced Concrete Bridges

Hui Zuo [1], Rodrigo Cespedes [2], Yeimi Zaldivar [3], Daniel O. X. Medina [3], Luis A. Bedriñana [3], José Fiestas [2], Nima Shirzad-Ghaleroudkhani [1,*] and Qipei Mei [1]

[1] Department of Civil and Environmental Engineering, University of Alberta, Edmonton, AB T6G 1H9, Canada; polo.huizuo@ualberta.ca (H.Z.)
[2] Department of Computer Science, Universidad de Ingeniería y Tecnología (UTEC), Lima 15063, Peru
[3] Department of Civil and Environmental Engineering, Universidad de Ingeniería y Tecnología (UTEC), Lima 15063, Peru
* Correspondence: shirzadg@ualberta.ca

Abstract

Accurate crack width measurement is essential for the condition assessment of reinforced concrete (RC) bridges, yet most unmanned aerial vehicle (UAV) inspections remain limited to pixel-level observations that cannot be converted into reliable metric units without an external scale reference. This paper presents a lightweight, drone-agnostic UAV-mounted metrology system that enables standards-aligned metric crack width measurement directly from inspection imagery. The payload integrates a focusable diffractive optical element (DOE) red laser that projects a cross pattern of known angular geometry, three TF-Luna time-of-flight (ToF) distance sensors, and an ESP-WROOM-32 microcontroller that provides dual-rate sampling, Bluetooth Low Energy (BLE) streaming, and on-board logging. A two-stage calibration links the synchronized distance measurements to the physical length of the projected cross, yielding an image-specific pixel-to-millimeter scale that is applied to pixel-level crack widths obtained from a vision-based segmentation pipeline. The system is field-deployed on the Puente Huamani Bridge in Pisco, Peru, where measurements of 39 cracks classified under AASHTO MBEI condition states are compared against independent manual measurements by six inspectors. The proposed system reduces measurement variability across all condition states (CS), lowering the average coefficient of variation from 0.36 to 0.10 for fine CS1 cracks, from 0.27 to 0.11 for CS2, and from 0.22 to 0.07 for CS3. Cross-platform adaptability is demonstrated through an additional deployment on a DJI Matrice 350 RTK at the Low Level Bridge in Edmonton, Canada. The results indicate that the system provides a practical, low-cost, and scalable solution for repeatable, standards-aligned UAV-based bridge crack assessment.

Keywords: crack width measurement; bridge inspection; unmanned aerial vehicle; metrology; laser scale reference; pixel-to-millimeter calibration; structural health monitoring

Academic Editor: Steve Vanlanduit

Received: 25 June 2026
Revised: 14 August 2026
Accepted: 19 August 2026
Published: 21 August 2026

1. Introduction

Reinforced concrete (RC) bridges are critical components of transportation networks, and ensuring their safety throughout their service life is essential [1,2]. Cracking is among the earliest and most diagnostically important visible indicators of deterioration in these structures [3]. Surface cracks compromise durability and strength by allowing the ingress

 https://doi.org/10.3390/metrology6030058

of water, carbon dioxide, and chlorides, which accelerate reinforcement corrosion and concrete degradation [4,5]. Consequently, controlling the initiation and propagation of cracks depends on their early and accurate detection [6]. Crack width is a particularly significant parameter, as it is used to assign condition states and to guide maintenance decisions through standardized width thresholds, such as those outlined in the AASHTO Manual for Bridge Element Inspection (MBEI) [7].

Despite the central role of crack width, conventional inspection remains heavily dependent on manual visual assessment, which presents several challenges [8]. Inspectors are often required to work at height or in hazardous environments, which raises significant safety risks [9]. Furthermore, the use of cranes, scaffolding, or under-bridge units, combined with traffic closures, results in high operational costs and extended inspection times [10]. Manual crack width estimation is further influenced by inspector judgment, viewing angle, and illumination, introducing substantial measurement variability [11].

To reduce inspection effort and extend coverage to difficult-to-access regions, unmanned aerial vehicles (UAVs) have been increasingly adopted for close-range bridge inspection [12,13]. As Waqas et al. [14] note, UAVs overcome accessibility difficulties without heavy machinery while reducing cost and increasing inspection frequency, enabling rapid image collection of deck soffits, piers, and bearings that would otherwise require traffic control or specialized access equipment [15]. The maturation of high-resolution camera payloads, photogrammetric reconstruction, and obstacle-aware flight now support increasingly routine aerial bridge inspection [16].

In parallel, computer vision has advanced rapidly for automated crack assessment. Early approaches relied on image-processing techniques such as edge detection [17], thresholding [18], and wavelet analysis [19], but these methods are sensitive to noise and illumination [20]. Deep learning has since enabled automatic feature extraction directly from raw images. Crack analysis methods currently fall into three categories: image classification for crack identification [21,22], bounding-box detection [23,24], and pixel-level semantic segmentation [25–28]. Within segmentation, fully convolutional and encoder–decoder designs have markedly improved the delineation of thin cracks against complex backgrounds. Yang et al. [29] developed a fully convolutional network for pixel-level crack measurement, Liu et al. [30] proposed a deeply supervised hierarchical architecture (DeepCrack) for end-to-end crack segmentation, and Manjunatha et al. [31] introduced a dense-connection backbone, CrackDenseLinkNet, that improves segmentation of cracks on concrete surfaces. The present work builds on this last approach for pixel-level crack extraction.

Despite this progress, a persistent barrier separates pixel-level detection from engineering-grade assessment: converting measurements from pixels to physical units [32]. Damage severity cannot be compared against standardized width thresholds unless each pixel measurement is associated with a reliable metric scale [33]. In UAV imagery, this scale is not fixed—it varies with standoff distance and camera pose, both of which change during flight [34]. Therefore, ensuring a geometrically consistent pixel-to-physical relationship within and between images remains a key limitation of quantitative inspection pipelines [35].

Three broad strategies have been used to recover a metric scale in image-based crack measurement. The first attaches a physical reference, such as a ruler, printed fiducial marker, or planar target, to or near the surface [36,37]. While accurate, this reintroduces the need for physical access to the very locations that UAVs are meant to reach remotely. The second strategy estimates scale from camera intrinsic together with an independently measured standoff distance [33,38]. Such photogrammetric approaches are powerful but sensitive to camera-specific calibration, focus breathing, and pose estimation, and they require platform-specific integration that is difficult to transfer between UAV models. The third strategy projects an active optical reference of known geometry onto the surface and infers scale from its imaged size [39–41]. Laser-based references are attractive because they are self-contained, require no contact with the structure, and can be read directly from the inspection image [42]. Nyathi et al. demonstrated millimeter-level crack width measurement using a projected laser beam without camera parameters or attached markers [39]; Zhao et al. combined a laser rangefinder with image processing to recover pixel scale and correct for non-perpendicular photography [40]; and Park et al. combined structured light with deep learning detection, accounting for laser alignment as the standoff varied [41].

These laser-based methods establish the feasibility of marker-free metric measurement, but several practical gaps remain for operational deployment. Single-beam references provide a scale but limited information about surface orientation; although some approaches attempt to compensate for non-perpendicular viewing [41,43], a single projected feature cannot fully recover the surface plane, so oblique imaging, unavoidable when a UAV cannot position itself normal to a pier or soffit, can introduce uncorrected error. Existing systems are often built around a specific camera or airframe [35,44], which complicates migration between the lightweight UAVs used for confined spaces and the industrial platforms used for long spans. Finally, the embedded sensing and data-handling architecture that makes such a system usable in the field, including synchronized multi-sensor acquisition, robust wireless transfer, and a repeatable calibration procedure, is decisive for real-world reliability, yet is seldom documented in sufficient detail to be reproduced.

This paper addresses these gaps with a lightweight, drone-agnostic UAV-mounted metrology system for standards-aligned metric crack width measurement, expanding on the preliminary system we presented at IABMAS 2026 [45]. The payload couples a diffractive optical element (DOE) laser that projects a cross pattern with three time-of-flight (ToF) distance sensors and an embedded microcontroller, paired with a desktop calibration application. The projected cross provides an active scale reference in every frame; the three spatially separated distance measurements provide redundancy and surface-orientation information; and a two-stage calibration links the measured standoff distance to the physical length of the projected cross, producing an image-specific pixel-to-millimeter scale. When applied to pixel-level crack widths from a vision-based segmentation pipeline [46], the system yields metric crack widths directly comparable with AASHTO MBEI condition state thresholds [7]. The principal contributions of this work are:

- A self-contained, low-cost (~190 g) metrology payload providing marker-free, image-specific metric scaling, mountable on UAV platforms from lightweight to industrial-grade without modification;
- An embedded firmware and data acquisition architecture with dual-rate sampling, mixed-interface multi-sensor integration, a reliability-oriented BLE transfer protocol, host-to-device clock synchronization, and on-board logging;
- A two-stage calibration methodology comprising a sensor tilt angle model and a laser cross length-to-distance scale relationship, implemented in a field-deployable tool;
- Field evaluation on the Puente Huamani Bridge (Peru) against six independent inspectors, plus cross-platform deployment on a DJI Matrice 350 RTK at the Low Level Bridge (Canada).

The remainder of the paper is organized as follows. Section 2 describes the materials and methods, including the system concept and hardware (Section 2.1), the embedded firmware and data acquisition architecture (Section 2.2), the two-stage calibration methodology (Section 2.3), the integration with the vision-based measurement pipeline (Section 2.4), and the field-deployment protocols (Section 2.5). Section 3 reports the calibration, measurement variability, accuracy, and cross-platform results. Section 4 discusses the findings, error sources, and limitations, and Section 5 concludes the paper and outlines directions for future work.

2. Materials and Methods

2.1. System Concept and Hardware Design

The proposed metrology system is designed to provide an image-specific metric scale for crack width measurement during routine UAV bridge inspection. The governing concept is to combine an active optical reference with synchronized distance sensing so that pixel-level image measurements can be converted into physical dimensions under realistic field conditions, without attaching any reference to the structure. The system is realized as a low-cost, lightweight, drone-agnostic payload that mounts on a range of UAV platforms without requiring modification to the onboard avionics or flight-control system.

As shown in Figure 1, the payload integrates four functional subsystems into a single assembly: a laser projection module, a distance-sensing module, a microcontroller and data acquisition unit, and a compact power supply. The laser module is a focusable red DOE projector that produces a cross-shaped pattern of known angular geometry. Because the angular spread of the projected cross is fixed by the diffractive element, the physical length of the cross on the target surface is a deterministic function of the standoff distance. The cross therefore acts as an active scale reference that is recorded in every captured frame. The cross pattern is selected over single dots or a single line because its two orthogonal arms provide symmetry, partial robustness to occlusion, and two independent length measurements that can be averaged to reduce reading noise.

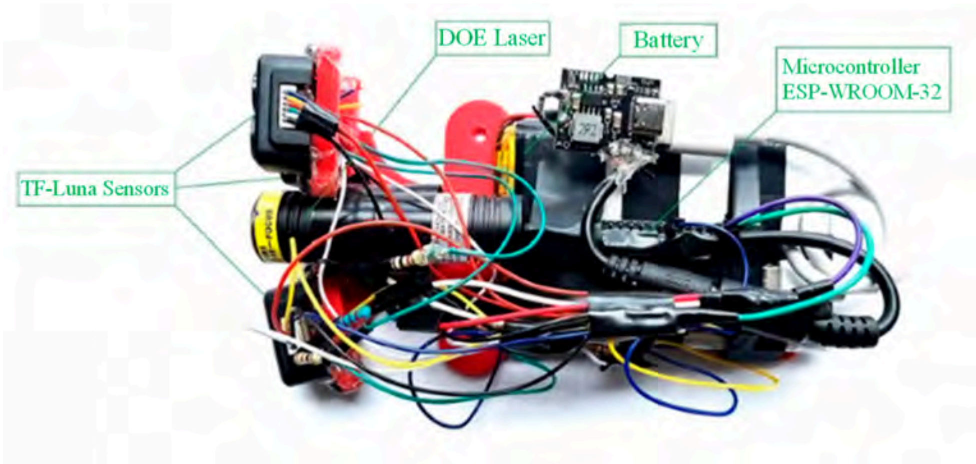

Figure 1. Assembled UAV-mounted metrology payload integrating the DOE laser projector, the three-sensor distance module, the ESP-WROOM-32 microcontroller, and the power supply on the 3D-printed mounting base.

Distance sensing and data acquisition are handled by an ESP-WROOM-32 microcontroller (Espressif Systems, Shanghai, China). The microcontroller interfaces with three TF-Luna ToF distance sensors that provide independent range measurements to the target surface. The physical pin numbering of the TF-Luna sensors is shown in Figure 2, and the corresponding pin functions and connection options are listed in Table 1. Two of the sensors are configured in UART-mode by tying the configuration pin to 3.3 V, while the third is configured in I^2C-mode by grounding the configuration pin. This mixed-interface arrangement allows three sensors to be serviced simultaneously by a single microcontroller while avoiding the address conflict that would arise from operating multiple TF-Luna units on a shared I^2C bus at the same default address.

The electrical connections between the microcontroller, the three TF-Luna sensors, and the supporting resistor network are shown in Figure 3. The resistor network supports the mixed communication interfaces and maintains stable signal levels during operation. The three sensors are mounted in a fixed spatial arrangement so that they sample three separated points on the target surface. This configuration improves robustness to local surface irregularities and, as detailed in Section 2.3, allows the orientation of the surface relative to the payload to be recovered, so that the true normal standoff distance can be estimated even when the camera axis is not perpendicular to the surface.

Figure 2. TF-Luna ToF sensor pins.

Table 1. Function and connection description of the TF-Luna ToF sensor pins.

NO.	Function	Description
1	+5V	Power supply
2	RXD/SDA	Receiving/Data
3	TXD/SCL	Transmitting/Clock
4	GND	Ground
5	Configuration Input	Ground: I2C mode Disconnected/3.3V: Serial port Communications mode
6	Multiplexing output	On/off mode: Output I2C mode: Data ready signal

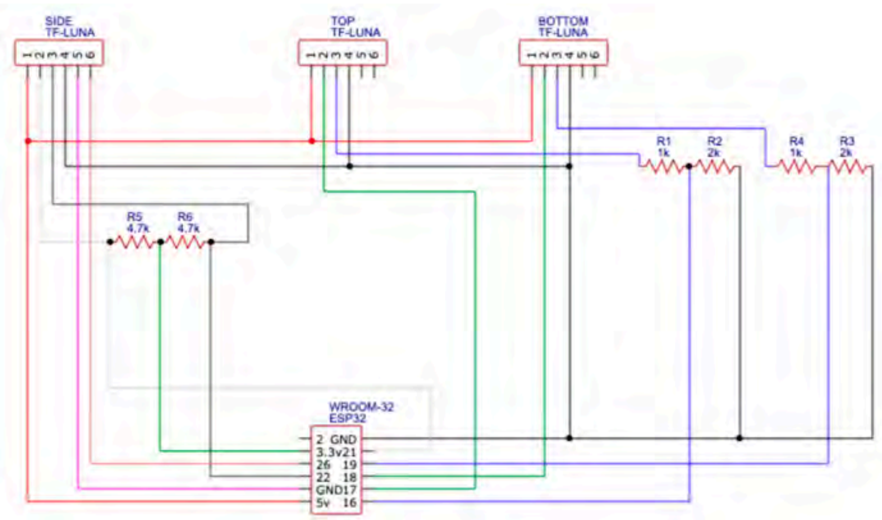

Figure 3. Wiring schematic of the sensor module, showing the two UART-mode and one I^2C-mode TF-Luna sensors, the resistor network, and the ESP-WROOM-32 connections.

All components are housed within a custom 3D-printed mounting base, shown in Figure 4, which fixes the relative geometry between the laser projector, the distance sensors, and the UAV camera. Fixing this geometry is essential: the calibration described in Section 2.3 is only transferable between deployments if the lever-arm offsets between the sensors and the laser remain constant. The base is printed in PLA on a desktop fused-deposition-modeling printer, which allowed for rapid, low-cost iteration of the mount geometry and made it straightforward to produce platform-specific adapters. The mount is drone-agnostic by design: it incorporates adjustable mounting features that accommodate the different hole spacings of different UAVs. Specifically, the center-to-center mounting-hole spacing D is 57.0 mm for the DJI Mavic 3E (DJI, Shenzhen, China) and 78.0 mm for the DJI Matrice 350 RTK (DJI, Shenzhen, China), both of which are supported by the same base design through interchangeable adapter plates.

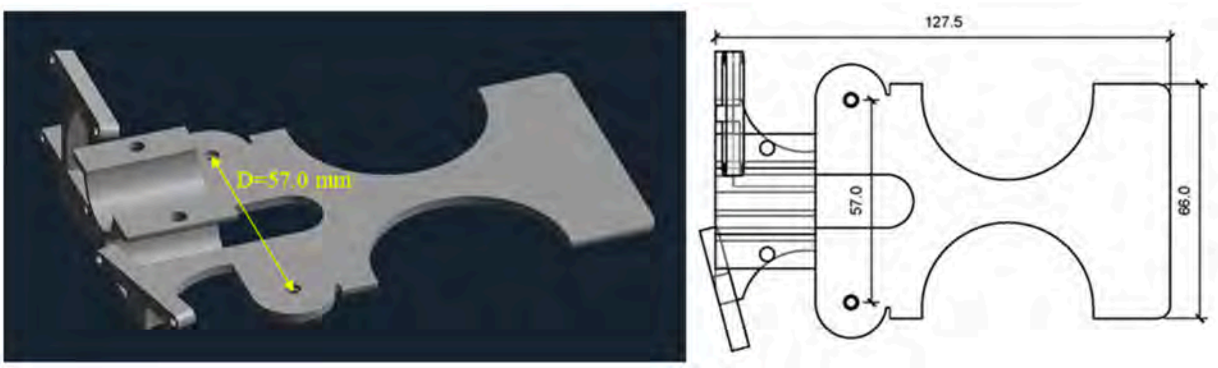

Figure 4. 3D-printed drone-agnostic mounting base (dimensions in mm), configured here for the DJI Mavic 3E.

The laser module operates at an optical output power of 150 mW (see Table 2), chosen to keep the projected cross visible against daylight-illuminated concrete at the operational standoff range while remaining within the payload power budget. The system is powered by an onboard 5000 mAh battery, making it electrically independent of the UAV. The total mass of the assembled payload, including the laser, sensor module, microcontroller, wiring, battery, and mounting base, is approximately 190 g. This mass is small relative to the payload capacity of both the lightweight Mavic 3E and the industrial Matrice 350 RTK, allowing deployment on either lightweight or industrial platforms without materially affecting flight endurance or handling.

Table 2. Key specifications of the UAV-mounted metrology payload.

Component/Property	Specification
Optical reference	Focusable red DOE laser, cross pattern, 150 mW
Distance sensors	3 × TF-Luna ToF (2 × UART, 1 × I^2C)
Microcontroller	ESP-WROOM-32 (dual-core, BLE)
Wireless link	Bluetooth Low Energy (BLE)
Internal sampling rate	100 Hz (per sensor)
Logging rate	2 Hz (configurable)
Power supply	Onboard 5000 mAh battery
Mounting base	3D-printed PLA, drone-agnostic adapters
Mount hole spacing D	57.0 mm (Mavic 3E)/78.0 mm (Matrice 350 RTK)
Total payload mass	≈190 g
Tested platforms	DJI Mavic 3E; DJI Matrice 350 RTK

2.2. Embedded Firmware and Data Acquisition Architecture

The metrology payload is governed by embedded firmware running on the ESP-WROOM-32 microcontroller, supported by a lightweight desktop application described in Section 2.3. The firmware is responsible for acquiring distance measurements from the three TF-Luna sensors, timestamping and buffering them, and transferring them reliably to a host computer. Its design reflects the practical constraints of bridge inspection, where wireless links are intermittent, flights are short, and the operator's attention is on flying rather than on monitoring data. Figure 5 summarizes the data acquisition and transfer architecture.

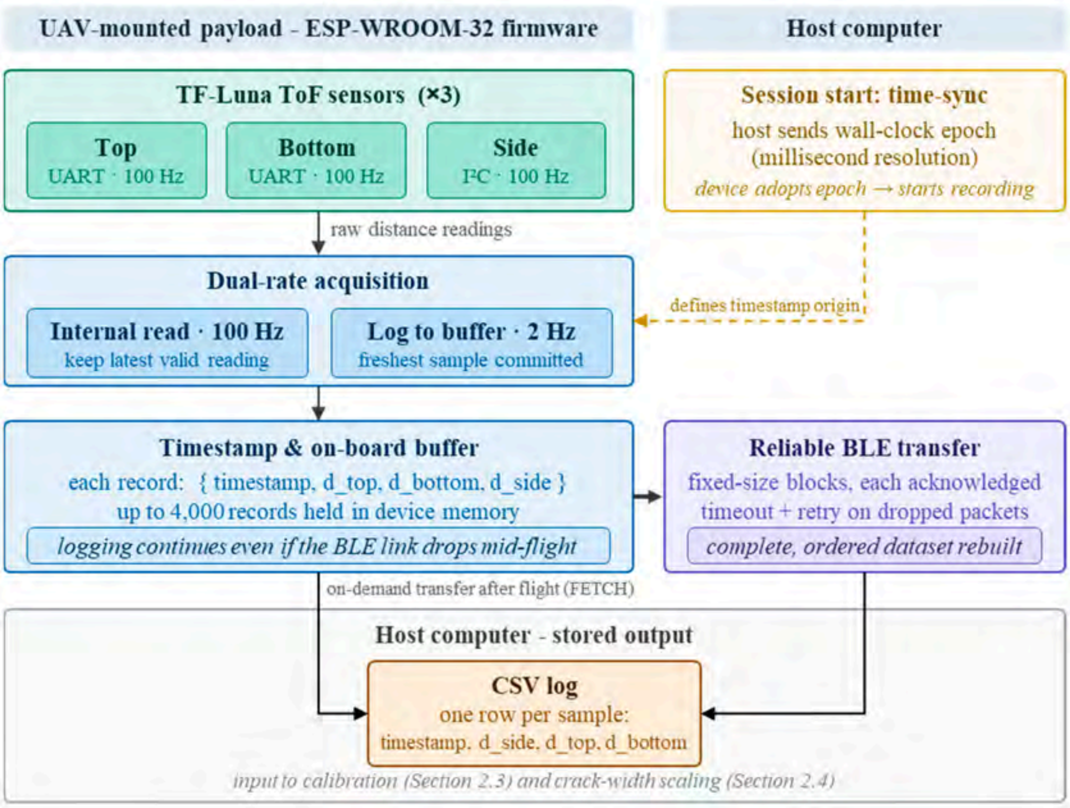

Figure 5. Embedded data acquisition and transfer architecture: dual-rate sampling of the three ToF sensors, on-board timestamped buffering, and the BLE block transfer protocol with per-block acknowledgement between the microcontroller and the host calibration tool.

2.2.1. Dual-Rate Sampling and Multi-Sensor Integration

The firmware separates the rate at which sensors are read from the rate at which data are logged. Each TF-Luna sensor is polled internally at a high rate of 100 Hz, and the most recent valid reading from each sensor is retained. Readings are committed to the data buffer at a lower, configurable logging rate, 2 Hz by default. Decoupling the two rates ensures that each logged sample reflects the freshest available reading from every sensor and that a transient dropout on one channel does not stall acquisition on the others. The two UART-mode sensors are parsed using the standard nine-byte TF-Luna frame, with frame-header validation to reject corrupted packets, while the I^2C-mode sensor is read from its distance registers; invalid or out-of-range returns are flagged and discarded rather than logged as zero, which preserves the integrity of the subsequent calibration statistics.

2.2.2. Time Synchronization and On-Board Logging

Because crack measurement requires associating each distance sample with the corresponding inspection image, the firmware supports host-to-device time synchronization. At the start of a recording session, the host transmits a synchronization message containing the current wall-clock time to millisecond resolution; the microcontroller adopts this epoch and timestamps every subsequent sample relative to it using its internal millisecond clock. Each buffered record stores a timestamp together with the three sensor readings. Critically, all samples are logged to on-board memory regardless of the wireless link state; thus, continuous connectivity is not required during flight. Live streaming over BLE is used during setup and short-range operation for monitoring, but the inspection of a large-span bridge does not impose a continuous communication constraint on the metrology system. After a flight, the buffered data are transferred to the host on demand.

2.2.3. Reliable BLE Block Transfer Protocol

Wireless data transfer uses BLE, which avoids additional cabling and does not interfere with UAV avionics. To make the transfer robust to the packet loss and intermittent connectivity common in the field, the firmware implements an explicit block transfer protocol driven by a finite-state machine. Buffered samples are transmitted in fixed-size blocks; after each block, the device enters a wait-for-acknowledgement state and pauses until the host returns an acknowledgement (ACK) for that block, after which it advances to the next block. A short inter-sample delay within each block prevents overrunning the host's receive buffer. When all blocks have been sent, the device issues a final marker and waits for a closing acknowledgement before returning to idle. Acknowledgement timeouts are handled gracefully: if an expected ACK does not arrive within a bounded interval, the device leaves the transfer state rather than blocking indefinitely. The host side mirrors this protocol, issuing per-block acknowledgements and a final acknowledgement, and writing each received record to a comma-separated value (CSV) file for downstream analysis. This handshake-and-recovery design ensures that a complete, ordered dataset is reconstructed at the host even when individual packets are delayed or dropped. Additional service commands allow the host to reset the buffer, set the buffer size and logging rate, and query the available device memory so that the maximum recordable session length can be displayed to the operator before a flight.

2.3. Two-Stage Calibration Methodology

Converting a pixel measurement into a physical crack width requires two pieces of information for each inspection image: the true normal standoff distance from the camera to the surface, and the physical length on the surface that corresponds to the imaged laser cross. The system obtains both from the same set of synchronized ToF measurements through a two-stage calibration. The first stage models the fixed tilt of the distance sensors so that the true normal standoff distance can be recovered from the raw readings; the second stage relates that standoff distance to the physical length of the projected cross, which, together with the cross length measured in pixels, yields the image-specific pixel-to-millimeter scale. The complete workflow is illustrated in Figure 6, and calibration is performed using the desktop tool described in Section 2.3.4.

2.3.1. Stage 1—Sensor Tilt Angle Geometric Model

The three TF-Luna sensors are mounted in a fixed geometry on the payload (see Figure 7). One sensor (denoted the bottom sensor) is aligned with the intended camera normal and measures the standoff distance z along that axis. The remaining two sensors (denoted the side and top sensors) are deliberately mounted at small fixed tilt angles relative to the normal axis, so that they sample points offset from the camera axis.

For a planar target oriented normal to the camera axis, a sensor tilted by an angle θ measures a slant range r related to the normal standoff distance by $r = z/\cos\theta$, so that the tilt angle of each off-axis sensor can be recovered from paired readings as

$$\theta = \arccos(z/r) \tag{1}$$

where z is taken from the on-axis (bottom) sensor and r is the reading of the tilted sensor. During calibration the laser cross is projected onto a planar surface at a series of known standoff distances; at each distance, synchronized readings are collected from all three sensors and Equation (1) is evaluated for the side and top sensors. Averaging over the calibration distances yields a stable estimate of each sensor's tilt angle, θ_{side} and θ_{top}. The fixed lever-arm offsets between the sensors, approximately $\Delta x \approx -62$ mm for the side sensor and $\Delta y \approx 25$ mm for the top sensor in the present build, are recorded alongside the angles. Once these parameters are known, the three slant ranges measured in the field determine the local surface plane: any inconsistency between the readings indicates that the surface is not normal to the camera axis, and the calibrated geometry allows the true normal standoff distance to be recovered rather than naively assuming the on-axis reading. This is the mechanism by which the three-sensor arrangement corrects for the oblique imaging that is unavoidable when a UAV cannot place its camera perpendicular to a pier or soffit.

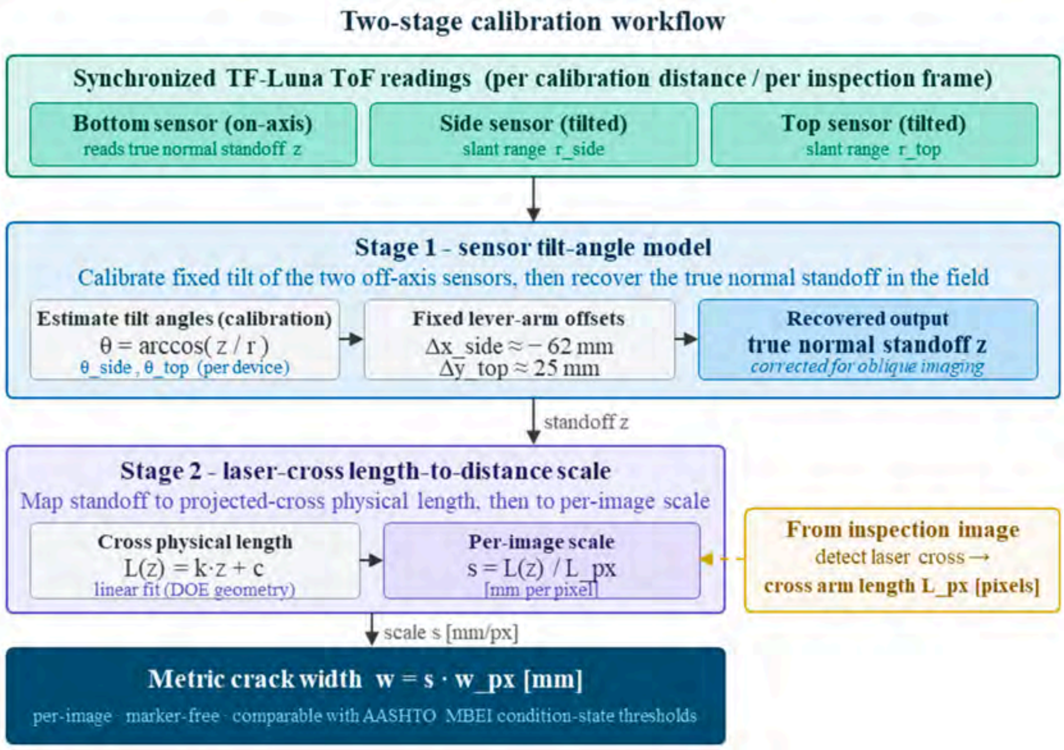

Figure 6. Two-stage calibration workflow: (Stage 1) recovery of the true normal standoff distance from the tilted ToF sensor readings via the tilt angle model; (Stage 2) mapping of standoff distance to projected-cross physical length and, with the imaged cross length, to the per-image pixel-to-millimeter scale.

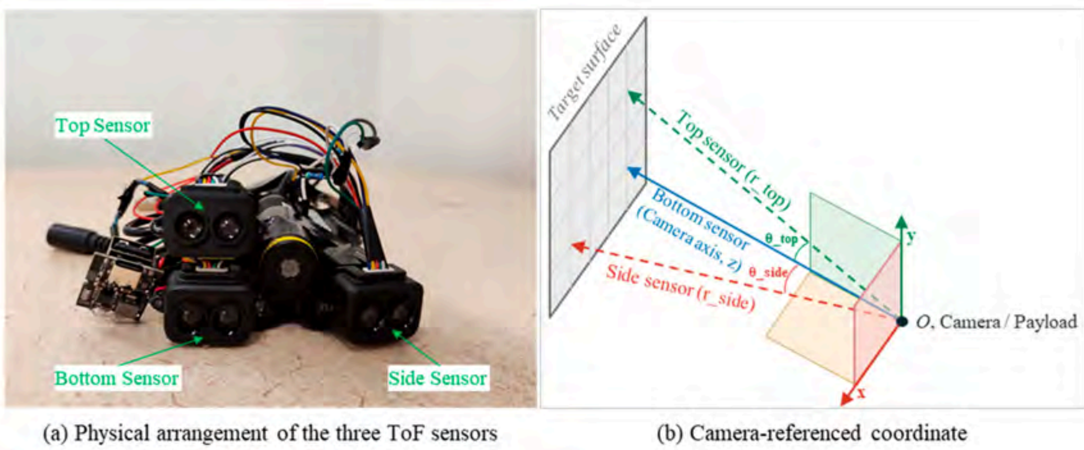

Figure 7. Sensor configuration and reference frame of the UAV-mounted metrology payload: (**a**) Physical arrangement of the three Time-of-Flight (ToF) distance sensors within the payload; (**b**) Schematic illustration of the camera-referenced coordinate system.

2.3.2. Stage 2—Laser Cross Length-to-Distance Scale

Because the angular geometry of the DOE cross is fixed, the physical length L of each arm of the projected cross on a planar surface grows linearly with the normal standoff distance

$$L(z) = k \cdot z + c \tag{2}$$

where the slope k is governed by the diffraction half-angle and the intercept c absorbs small fixed offsets in the optical path. The coefficients k and c are determined empirically during the same calibration session: at each known standoff distance, the recovered normal distance from Stage 1 is paired with the physical cross length, and a linear relationship is fitted by least squares. In an inspection image, the laser cross is detected and its arm length is measured in pixels, L_{px}; the synchronized ToF measurement provides the standoff distance z, from which the physical cross length $L(z)$ is obtained. The image-specific pixel-to-millimeter scale is then

$$s = L(z)/L_{px} \text{ [mm/pixel]} \tag{3}$$

and the metric width of a crack is recovered by multiplying its pixel width w_{px} by the scale, $w = s \cdot w_{px}$. Because s is computed independently for each image from that image's own laser cross and its own synchronized distance reading, the method is inherently adaptive to the changing standoff distance and pose of UAV operation and does not rely on fixed camera intrinsic or any reference attached to the structure.

2.3.3. Bias Estimation and Error Checking

To verify sensor accuracy before a calibration is exported, the tool includes a bias estimation routine. With the payload held at a known true distance, a short synchronized burst is recorded and the mean reading of each sensor is compared against the operator-supplied reference distance to yield a per-sensor bias in millimeters. This check detects gross misconfiguration, such as a sensor reading in the wrong mode or an obstructed aperture, and quantifies the residual offset of each channel, which can be subtracted during analysis. The same routine is used in the field to confirm that the sensors behave consistently at the actual inspection standoff before image acquisition begins.

2.3.4. Field-Deployable Calibration Tool

The calibration workflow is implemented in a desktop application with a PyQt graphical interface that communicates with the payload over BLE. The tool guides the operator through device discovery and connection (with an option to remember a device for rapid reconnection), time synchronization, data collection into per-session CSV files, and parameter estimation. After a set of samples at known distances has been collected, the tool evaluates Equation (1) for the side and top sensors, plots the estimated tilt angle against the actual distance so that the operator can visually confirm consistency, and reports the mean tilt angles. The estimated angles, together with the recorded lever-arm offsets, are exported to a compact calibration file that is reused during inspection. Separating calibration from inspection in this way allows the same parameters to be applied across multiple flights and platforms, and it makes re-calibration in the field a matter of minutes. The complete firmware and calibration tool are central to the reproducibility of the system and are summarized in Figures 5 and 6.

2.4. Integration with the Vision-Based Measurement Pipeline

The metrology system supplies the metric scale; the spatial extent of each crack in pixels is provided by a vision-based crack detection and segmentation framework developed previously by the authors [46]. In that pipeline, UAV-acquired bridge images are processed by a deep learning classification and segmentation model trained on concrete bridge imagery, producing pixel-level crack masks from which local crack widths are measured along the crack centerline. The two components are combined per image: the laser cross in the image is detected and its arm length in pixels is measured; the synchronized ToF reading for that image is retrieved by timestamp; Stage 1 of the calibration recovers the normal standoff distance; Stage 2 converts it to the physical cross length and hence to the pixel-to-millimeter scale of Equation (2); and the scale is applied to the segmented pixel widths to yield metric crack widths. The resulting widths are directly comparable with the MBEI condition state thresholds [7] and with the manual reference measurements described next. Figure 8 illustrates this end-to-end conversion from a raw inspection image to a metric crack width.

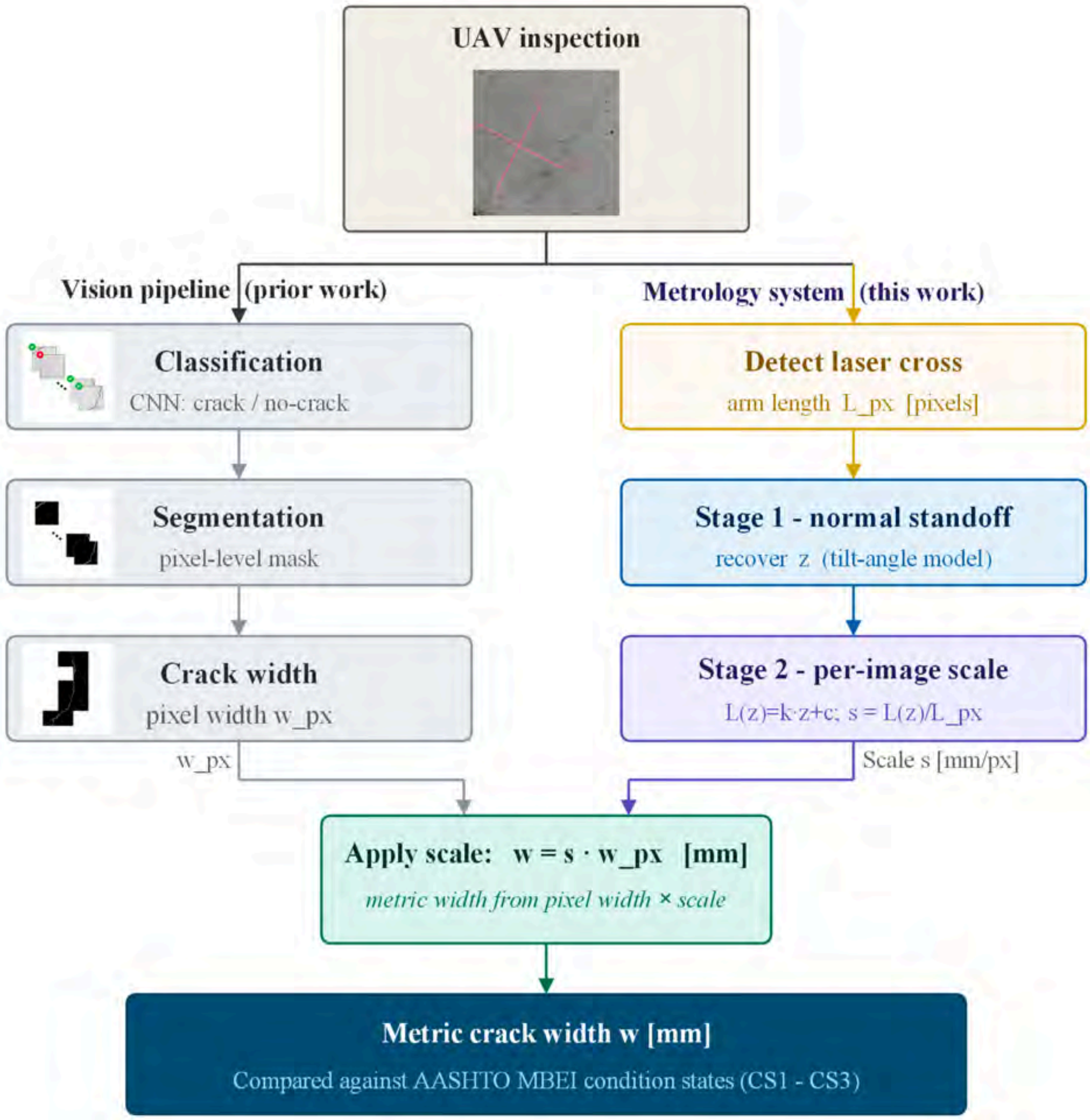

Figure 8. End-to-end measurement workflow, from a raw UAV image containing the projected laser cross, through laser cross detection and crack segmentation, to the image-specific pixel-to-millimeter scaling that produces a metric crack width.

2.5. Field Deployment and Experimental Setup

2.5.1. Primary Deployment: Puente Huamani Bridge, Pisco, Peru

Field validation is conducted on the Puente Huamani Bridge in Pisco, Peru (Figure 9). The bridge is a reinforced concrete structure spanning the Pisco River and is representative of a setting in which conventional inspection is difficult, because access to the substructure is limited. The site offers clear visibility of the deck soffit and pier surfaces while permitting safe UAV operation without interrupting traffic. Image acquisition is performed with a DJI Mavic 3E carrying the metrology payload described in Section 2.1. The UAV is flown beneath the deck and along the piers to capture high-resolution images of the concrete surfaces (Figure 10), under daylight conditions and within the operational standoff range of the laser and distance sensors. The projected DOE cross is visible in every inspection image and is recorded together with the synchronized TF-Luna measurements.

Figure 9. Puente Huamani Bridge in Pisco, Peru.

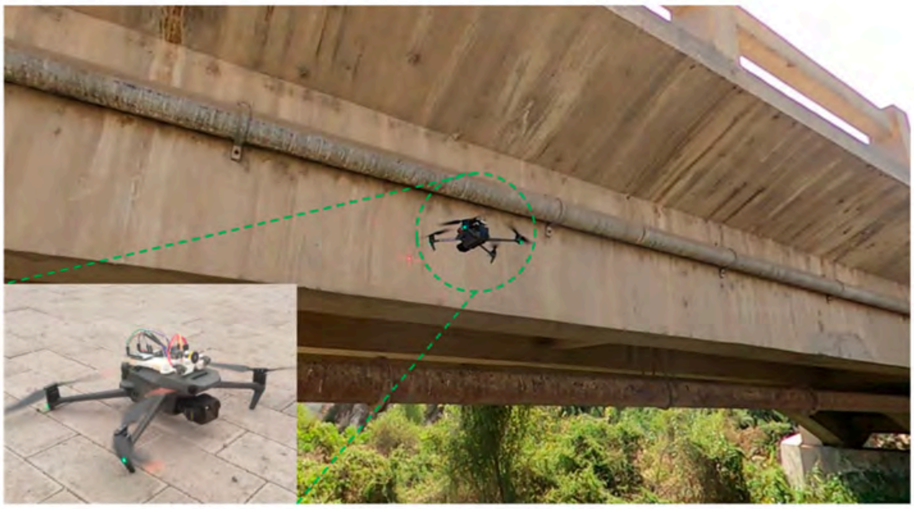

Figure 10. UAV-based field data acquisition beneath the bridge deck, with the DJI Mavic 3E carrying the metrology payload.

To establish a reference baseline, manual crack width measurements are carried out on the same bridge following the MBEI guidelines [7]. Six inspectors independently measured crack widths using standard inspection tools. Cracks are classified into condition states CS1 through CS3 according to the width thresholds for reinforced concrete elements summarized in Table 3. For each crack, the median of the six manual measurements is adopted as the representative reference value, reducing the influence of any single inspector's outlying reading.

Table 3. Condition state (CS) width definitions for reinforced concrete elements per the AASHTO MBEI.

Condition State	Reinforced Concrete (RC) Defect 1130—Crack Width
CS1 (Good)	Width < 0.012 in. (<0.3 mm)
CS2 (Fair)	Width 0.012–0.05 in. (0.3–1.27 mm)
CS3 (Poor)	Width > 0.05 in. (>1.27 mm)

2.5.2. Cross-Platform Deployment: Low Level Bridge, Edmonton, Canada

To evaluate the adaptability of the system across UAV platforms and field conditions, a second deployment is conducted at the Low Level Bridge in Edmonton, Canada (Figure 11). This site differs from Puente Huamani in several operationally significant ways: it spans a wider river, has taller piers, and offers reduced clearance beneath the deck, which together constitute a more demanding inspection scenario. The deployment also used a different and substantially larger aircraft, a DJI Matrice 350 RTK, in place of the Mavic 3E. The same metrology payload is mounted on the Matrice 350 RTK through the corresponding adapter of the drone-agnostic base (mounting-hole spacing D = 78.0 mm), without any modification to the payload electronics, firmware, or calibration parameters. The objective of this deployment is to evaluate platform transferability rather than to provide a second inspector-referenced accuracy benchmark: no multi-inspector manual measurement campaign was conducted at this site. The deployment instead confirms that stable laser projection, reliable multi-sensor distance acquisition, and consistent pixel-to-millimeter scaling are preserved when the identical payload and calibration are transferred to a different platform operating in a harder environment. Table 4 contrasts the two deployment sites and platforms.

Figure 11. Cross-platform field deployment at the Low Level Bridge in Edmonton, Canada, using the DJI Matrice 350 RTK carrying the same metrology payload.

Table 4. Comparison of the two field-deployment sites and UAV platforms.

Attribute	Puente Huamani Bridge	Low Level Bridge
Location	Pisco, Peru	Edmonton, Canada
UAV platform	DJI Mavic 3E	DJI Matrice 350 RTK
Mount spacing D	57.0 mm	78.0 mm
Span/clearance	Moderate	Wider span, taller piers, low clearance
Role	Primary validation	Cross-platform adaptability
Payload/calibration	Baseline	Identical, unchanged

3. Results

3.1. Calibration Results

The Stage 2 laser cross length-to-distance relationship is well described by the linear model L(z) = k·z + c over the operational standoff range of approximately 0.5–3.6 m. Least squares regression over the 16 calibration points spanning standoff distances from 0.49 m to 3.58 m yields L(z) = 0.2283·z + 2.261, with a coefficient of determination of R^2 = 0.99997. This near-ideal linearity is a geometric consequence of the fixed angular spread of the diffractive optical element, for which the projected cross length grows in direct proportion to distance; the high coefficient of determination therefore confirms linearity but does not by itself establish metrological accuracy.

To characterize the calibration more rigorously, the uncertainty of the fitted parameters is quantified. The fitted slope is 0.22833 with a standard error of 0.00033, corresponding to a relative standard error of 0.14% (95% confidence interval (CI) 0.22761–0.22904). The intercept is 2.261 mm with a standard error of 0.735 mm (95% CI 0.683–3.838 mm); this small positive offset is attributable to the lever-arm separation between the laser emission point and the reference plane of the ToF sensors, and its confidence interval excludes zero, indicating a consistent systematic offset rather than random scatter. The residual standard deviation (SD) of the fit is 1.24 mm.

As shown in Figure 12a, the 95% confidence band of the regression line and the 95% prediction band for individual observations are both narrower than the plotted line width at this scale, reflecting the tightness of the fit. The residuals, plotted against standoff distance in Figure 12b, are randomly distributed about zero with no systematic trend across the operational range, indicating that the linear model is adequate throughout; a single point at z = 2.33 m departs from the fit by 3.9 mm, which does not materially affect the fitted parameters. Propagating the prediction interval through the inverse relationship gives a 95% prediction uncertainty in the recovered standoff distance of approximately ±12 mm across the operational range.

The bias estimation routine confirmed that the residual per-sensor offsets are small relative to the crack widths of interest, ensuring that the three distance readings used to recover the normal standoff distance through the Stage 1 plane model are individually accurate.

3.2. Crack Measurement Variability

Measurement variability is evaluated by comparing the proposed system against the manual field measurements. Six inspectors independently measured 39 cracks on the Puente Huamani Bridge; for each crack, the median of the six manual readings served as the reference, and the cracks are grouped into condition states CS1–CS3. This benchmark reflects current field practice rather than a traceable reference, and the comparisons reported below therefore characterize agreement and relative dispersion with respect to conventional manual inspection rather than absolute accuracy. Representative measurement samples spanning the three condition states are shown in Figure 13. In each case, the metric width is obtained by applying the image-specific pixel-to-millimeter scale to the segmented pixel width. Five measurements are acquired per crack with the proposed system from different standoff distances while imaging the same reference location on the crack, so that the reported dispersion characterizes the consistency of the metric scaling across the operational standoff range. The comparison is summarized in Figure 14 and Table 5.

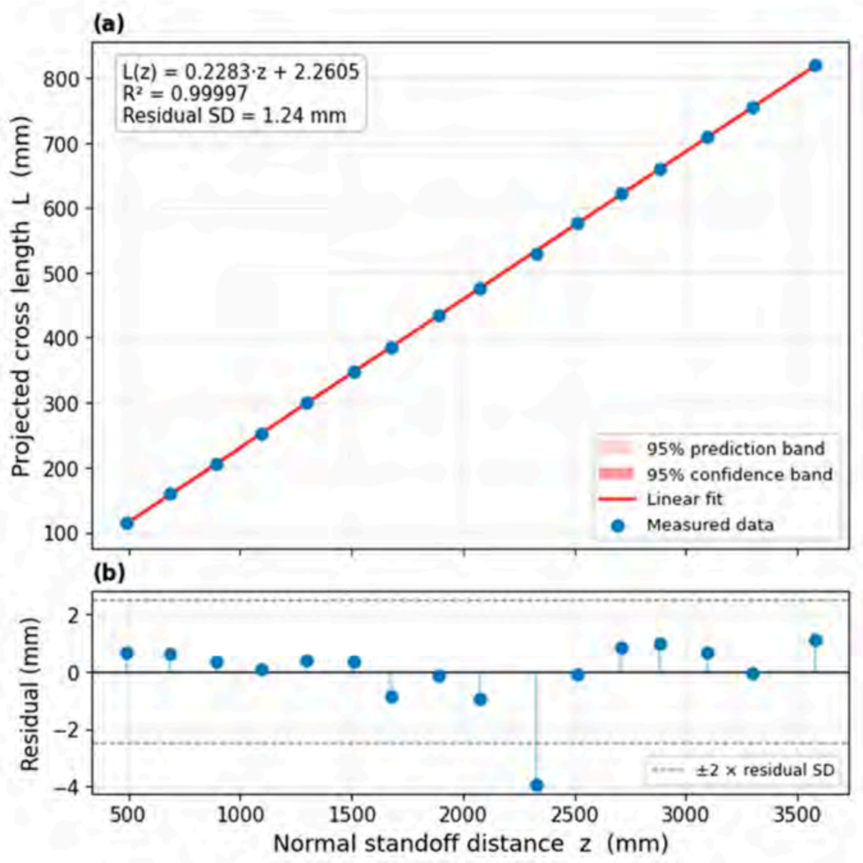

Figure 12. Calibration results and uncertainty analysis. (**a**) Projected laser cross length L versus normal standoff distance z. (**b**) Residuals of the fitted model plotted against standoff distance.

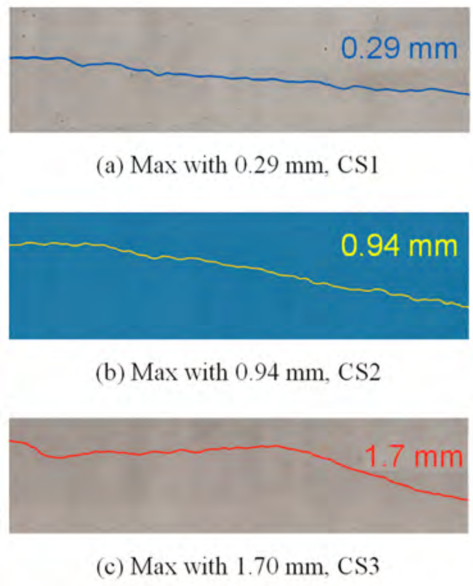

Figure 13. Representative measurement samples across condition states: (**a**) maximum crack width measurement of 0.29 mm for Condition State 1 (CS1); (**b**) maximum crack width measurement of 0.94 mm for Condition State 2 (CS2); (**c**) maximum crack width measurement of 1.70 mm for Condition State 3 (CS3).

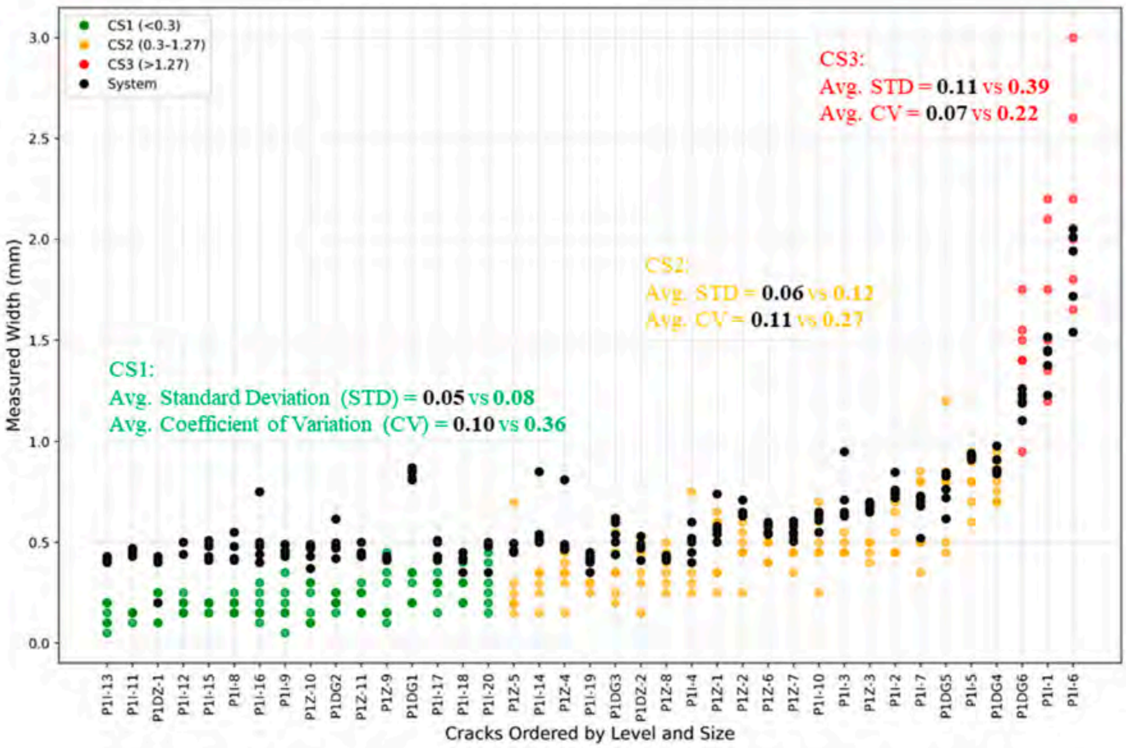

Figure 14. Crack measurement variability of the proposed system versus manual inspection across condition states CS1–CS3.

Table 5. Average measurement variability by condition state: proposed system versus manual inspection (39 cracks, six inspectors).

Condition State	Manual SD (mm)	Manual CV	System SD (mm)	System CV
CS1 (Good)	0.08	0.36	0.05	0.10
CS2 (Fair)	0.12	0.27	0.06	0.11
CS3 (Poor)	0.39	0.22	0.11	0.07

Manual inspection exhibited substantial variability, most pronounced for fine cracks. For the CS1 group, the average standard deviation (SD) across inspectors is 0.08 mm and the average coefficient of variation (CV) is 0.36. For CS2, the average SD rose to 0.12 mm with a CV of 0.27, and for CS3, the average SD reached 0.39 mm with a CV of 0.22. The trend confirms that manual crack width estimation is highly sensitive to inspector judgment and that the relative dispersion is greatest for the smallest cracks, precisely where condition state boundaries are tightest.

The proposed system produced consistently lower variability across all condition states. For CS1 cracks, the system achieved an average SD of 0.05 mm and an average CV of 0.10; for CS2, 0.06 mm and 0.11; and for CS3, 0.11 mm and 0.07. The reduction in CV is especially marked for fine cracks, where the system's relative variability is roughly a third of that of manual measurement. A slight tendency toward overestimation is observed for very fine cracks, and a small number of isolated cases showed noticeable absolute deviation from the manual reference; these are discussed in Section 4. Such deviations occurred predominantly within the fine-crack range, where the manual measurements themselves are highly dispersed.

A paired comparison across the 39 cracks is performed to assess the statistical significance of the observed differences. The dispersion of the proposed system is significantly lower than that of manual inspection: the mean paired difference in coefficient of variation is 0.199 (95% CI 0.154–0.243; paired t(38) = 9.05, $p < 0.001$; Wilcoxon $p < 0.001$;

Cohen's d_z = 1.45), and the corresponding difference in standard deviation is 0.068 mm (95% CI 0.039–0.097; $t(38) = 4.72$, $p < 0.001$; Wilcoxon $p < 0.001$; $d_z = 0.76$). Because the Shapiro–Wilk test indicated departure from normality for the paired differences ($p < 0.05$), the non-parametric results are reported alongside the parametric tests; both are concordant.

The same analysis identifies a systematic difference between the two methods. The system reports widths that are on average 0.163 mm larger than the manual median (95% CI 0.112–0.213; $t(38) = 6.55$, $p < 0.001$; Wilcoxon $p < 0.001$; $d_z = 1.05$). This offset is width-dependent: +0.284 mm for CS1 cracks, +0.128 mm for CS2, and −0.204 mm for the three CS3 cracks. Figure 15a presents a Bland–Altman agreement plot, in which the difference between the system and manual measurements is plotted against their mean for each crack. The differences are predominantly positive and vary systematically with crack width: CS1 cracks cluster near +0.3 mm, CS2 cracks near +0.1 mm, and the three CS3 cracks fall below zero, with the 95% limits of agreement spanning −0.14 mm to +0.47 mm. This width-dependent pattern, rather than a proportional fan, indicates an approximately constant offset whose relative significance is greatest for the finest cracks. Figure 15b compares the coefficient of variation for each crack, with a line connecting its manual and system values. Nearly every line slopes downward, and the system values form a markedly tighter cluster than the manual values, showing that the reduction in dispersion holds for individual cracks rather than only in aggregate.

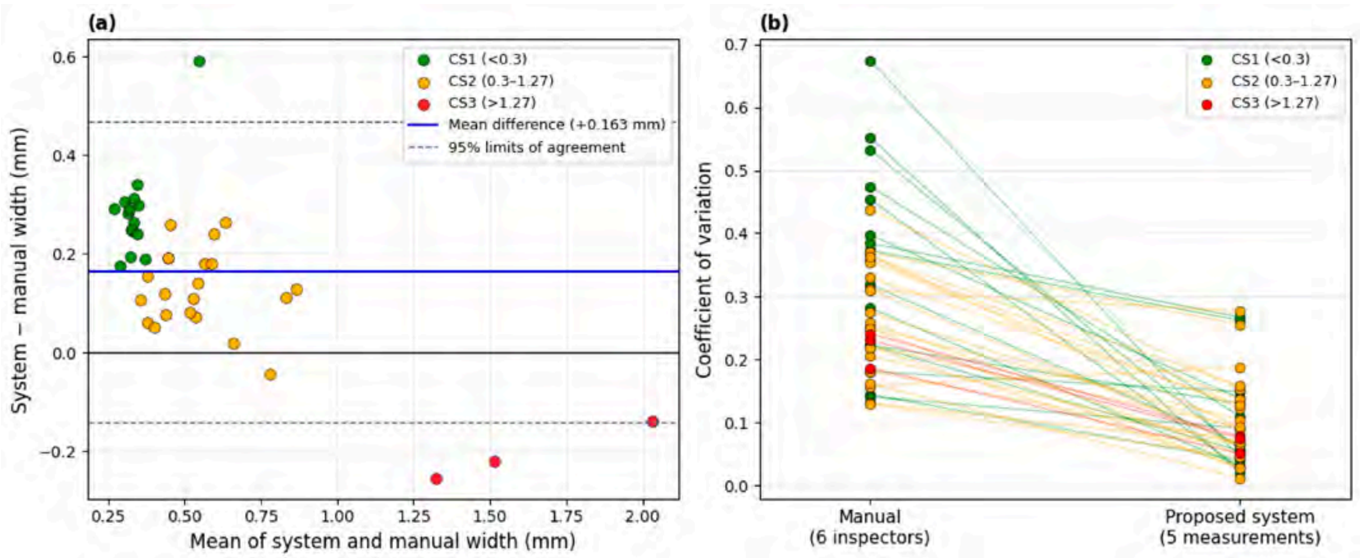

Figure 15. Paired statistical comparison between the proposed system and manual inspection across 39 cracks. (**a**) Agreement plot of the difference between the system measurement and the manual median against their mean. (**b**) Paired comparison of the coefficient of variation for each crack, with lines connecting the manual and system values.

4. Discussion

The results support the central proposition of this work: that a compact, marker-free optical-plus-ranging payload can deliver image-specific metric scaling that is both more repeatable than manual measurement and transferable across UAV platforms. Three aspects of the findings merit further discussion.

First, the consistent reduction in coefficient of variation across all condition states, and most strongly for fine CS1 cracks, reflects the structural advantage of an instrumented scale over human estimation. Manual crack width reading depends on the inspector's viewing angle, the resolution of the crack card or gauge, and subjective judgment at the crack edge, all of which compound for narrow cracks near the 0.3 mm CS1/CS2 boundary. By deriving the scale from a projected reference and a measured standoff distance in each image, the proposed system removes much of this subjectivity and yields tighter agreement between repeated measurements. This is consistent with the broader literature on laser- and structured light-based scaling, which has repeatedly found that an active reference improves the objectivity of millimeter-level crack quantification relative to pixel-only or marker-dependent methods [39,41,43].

Second, the overestimation observed for very fine cracks, quantified in Section 3.2 as a systematic offset of +0.284 mm for CS1 cracks that decreases to +0.128 mm for CS2 and reverses to −0.204 mm for CS3, locates the present accuracy limits of the system. The width dependence of this offset is itself informative: an error in the metric scaling would produce a deviation proportional to crack width, whereas the observed pattern is closer to a constant offset whose relative significance grows as cracks become finer. This is consistent with the segmentation pipeline over-segmenting extremely narrow cracks whose width approaches the imaging resolution, inflating the pixel width before scaling, rather than with an error in the laser-based scale recovery. Strong ambient illumination and highly textured concrete can reduce the contrast of the projected cross, introducing error into the measured cross length and hence the scale. Large viewing angles, although partially corrected by the three-sensor tilt model of Section 2.3.1, leave a residual error when the surface is both oblique and non-planar. Importantly, the cases with the largest deviations fell within the fine-crack range, where the manual reference is itself highly variable; in that regime, the manual median is an imperfect ground truth, and part of the apparent deviation reflects uncertainty in the reference rather than error in the system. These observations point to specific, addressable improvements rather than a fundamental limitation of the approach.

Third, the cross-platform deployment demonstrates a practical property that is often asserted but seldom shown: that the identical payload, firmware, and calibration can be moved between a lightweight and an industrial UAV and continue to perform in a more demanding environment. This transferability follows directly from two design decisions, fixing the sensor-laser geometry in a rigid 3D-printed base so that the calibration remains valid, and making the payload electrically and computationally self-contained so that it imposes no integration burden on the host aircraft. Together, these decisions decouple the metrology from the platform, which is what allows a single calibration to serve multiple aircraft.

The system also has limitations that bound its current applicability. The projected cross must be visible in the image, which constrains operation under very strong ambient light or at standoff distances beyond the laser's effective range; the linear cross-length model assumes a locally planar surface, so strongly curved or spalled regions are not fully captured by the present geometry; and the accuracy of the metric width inherits any error in the upstream segmentation. The reliance on a median of six manual measurements as the benchmark, while pragmatic, does not provide metrological traceability, and the deviations reported in Section 3.2 therefore conflate error in the proposed system with uncertainty in the benchmark itself. Establishing traceable accuracy will require validation against reference artifacts or a calibrated crack width instrument under controlled conditions. These limitations motivate the directions outlined in Section 5.

5. Conclusions

This paper presented a lightweight, drone-agnostic UAV-mounted metrology system that enables standards-aligned metric crack width measurement from bridge inspection imagery without attaching any reference to the structure. The payload integrates a focusable DOE laser projecting a cross of known angular geometry, three TF-Luna ToF distance sensors, and an ESP-WROOM-32 microcontroller providing dual-rate sampling, reliable BLE block transfer with acknowledgement and recovery, host-to-device time synchronization, and on-board logging. A two-stage calibration, comprising a tilt angle geometric model that recovers the true normal standoff distance from the three sensors and a laser cross length-to-distance relationship that yields the per-image scale, is implemented in a field-deployable tool and validated in the laboratory and the field. The main conclusions are:

- Image-specific pixel-to-millimeter scaling is achieved from a calibrated laser reference and synchronized distance measurements, enabling conversion of pixel-level crack widths into metric units suitable for standards-based assessment, with no reference attached to the structure.
- Across 39 cracks measured on the Puente Huamani Bridge, the proposed system reduced measurement variability relative to manual inspection in every condition state, with the largest relative improvement for fine CS1 cracks, where manual variability is greatest.
- The embedded firmware and two-stage calibration together form a self-contained, fully documented sensing module that can be independently reproduced and recalibrated in the field.
- Cross-platform adaptability is demonstrated by transferring the identical payload and calibration from a DJI Mavic 3E to a DJI Matrice 350 RTK in a more demanding environment, with stable laser projection, reliable distance sensing, and consistent scaling preserved without platform-specific modification.

Future work will focus on improving robustness under strong ambient lighting and on highly textured or non-planar surfaces, enhancing laser cross detection at large viewing angles, extending the geometric model beyond the locally planar assumption, and benchmarking the system against higher-accuracy optical and contact references across a wider range of bridge types. Tighter coupling between the metric scale and the segmentation stage, for example, using the recovered scale to guide sub-pixel edge localization, is also expected to reduce the residual overestimation observed for the finest cracks. Overall, the proposed metrology system offers a practical, low-cost, and scalable route to repeatable, standards-compliant metric crack measurement in UAV-based bridge inspection.

Author Contributions: Conceptualization, H.Z., L.A.B., J.F., N.S.-G. and Q.M.; methodology, H.Z., R.C., Y.Z., D.O.X.M., L.A.B., J.F., N.S.-G. and Q.M.; software, H.Z., R.C., Y.Z. and D.O.X.M.; validation, H.Z., R.C., Y.Z. and D.O.X.M.; formal analysis, H.Z., R.C., Y.Z. and D.O.X.M.; investigation, H.Z., R.C., Y.Z. and D.O.X.M.; resources, L.A.B., J.F., N.S.-G. and Q.M.; data curation, H.Z., R.C., Y.Z. and D.O.X.M.; writing—original draft preparation, H.Z.; writing—review and editing, H.Z., R.C., Y.Z., D.O.X.M., L.A.B., J.F., N.S.-G. and Q.M.; visualization, H.Z. and Y.Z.; supervision, L.A.B., J.F., N.S.-G. and Q.M.; project administration, L.A.B. and N.S.-G.; funding acquisition, L.A.B., J.F., N.S.-G. and Q.M. All authors have read and agreed to the published version of the manuscript.

Funding: This research was funded by the 2024 University of Alberta—Universidad de Ingeniería y Tecnología (UTEC) Seed Grant Program.

Data Availability Statement: The measurement data presented in this study are provided in Appendix A.

Acknowledgments: The authors gratefully acknowledge the support of the 2024 University of Alberta—Universidad de Ingeniería y Tecnología (UTEC) Seed Grant Program, and thank the inspection personnel who participated in the field measurements. This article is a revised and expanded version of a paper entitled "A UAV-Mounted Metrology System for Accurate Crack Measurement in Bridges," which was presented at the Thirteenth International Conference on Bridge Maintenance, Safety and Management (IABMAS 2026), Orlando, FL, USA, 7–10 July 2026.

Conflicts of Interest: The authors declare no conflicts of interest.

Appendix A

Table A1. Manual crack width measurements for the primary deployment. For each of the 39 cracks, the table lists the width recorded by each of the six independent inspectors, together with the median, standard deviation (SD), and coefficient of variation (CV) across inspectors, and the assigned AASHTO MBEI condition state (CS). Each inspector's value is the maximum of the readings taken at the location judged to be widest. All widths are in millimeters; CV is dimensionless. Inspector identities have been anonymized.

No.	Crack ID	Insp. 1	Insp. 2	Insp. 3	Insp. 4	Insp. 5	Insp. 6	Median	SD	CV	CS
1	P1DG1	0.35	0.20	0.30	0.20	0.20	0.35	0.25	0.075	0.282	CS1
2	P1DG2	0.25	0.15	0.20	0.20	0.20	0.25	0.20	0.038	0.181	CS1
3	P1DG3	0.35	0.35	0.25	0.20	0.45	0.55	0.35	0.128	0.358	CS2
4	P1DG4	0.95	0.80	0.70	0.75	0.70	0.90	0.78	0.105	0.131	CS2
5	P1DG5	1.20	0.80	0.45	0.50	0.80	0.85	0.80	0.271	0.354	CS2
6	P1DG6	1.75	1.50	1.40	0.95	1.40	1.55	1.45	0.266	0.187	CS3
7	P1I-1	2.20	1.35	1.75	1.20	1.50	2.10	1.63	0.406	0.241	CS3
8	P1I-2	0.70	0.45	0.45	0.65	0.45	0.55	0.50	0.111	0.206	CS2
9	P1I-3	0.65	0.45	0.45	0.50	0.45	0.55	0.47	0.080	0.158	CS2
10	P1I-4	0.25	0.60	0.40	0.30	0.75	0.35	0.38	0.193	0.438	CS2
11	P1I-5	0.95	0.60	0.80	0.90	0.70	0.80	0.80	0.128	0.162	CS2
12	P1I-6	2.20	1.80	2.00	1.65	2.60	3.00	2.10	0.510	0.231	CS3
13	P1I-7	0.80	0.50	0.50	0.35	0.80	0.85	0.65	0.209	0.330	CS2
14	P1I-8	0.20	0.15	0.15	0.20	0.25	0.15	0.17	0.041	0.223	CS1
15	P1I-9	0.20	0.05	0.35	0.25	0.15	0.15	0.17	0.102	0.532	CS1
16	P1I-10	0.60	0.25	0.70	0.45	0.50	0.45	0.47	0.153	0.311	CS2
17	P1I-11	0.15	0.10	0.15	0.15	0.15	0.15	0.15	0.020	0.144	CS1
18	P1I-12	0.20	0.15	0.15	0.25	0.20	0.15	0.17	0.041	0.223	CS1
19	P1I-13	0.20	0.05	0.10	0.15	0.10	0.20	0.13	0.061	0.454	CS1
20	P1I-14	0.50	0.15	0.35	0.30	0.25	0.35	0.32	0.117	0.369	CS2
21	P1I-15	0.20	0.15	0.15	0.20	0.20	0.20	0.20	0.026	0.141	CS1
22	P1I-16	0.20	0.10	0.25	0.15	0.15	0.30	0.17	0.074	0.384	CS1
23	P1I-17	0.35	0.15	0.30	0.30	0.30	0.25	0.30	0.069	0.251	CS2
24	P1I-18	0.40	0.20	0.35	0.20	0.30	0.30	0.30	0.080	0.275	CS2
25	P1I-19	0.45	0.30	0.25	0.40	0.40	0.30	0.35	0.077	0.221	CS2
26	P1I-20	0.40	0.20	0.30	0.15	0.25	0.45	0.28	0.116	0.397	CS1
27	P1Z-1	0.60	0.25	0.35	0.60	0.35	0.65	0.47	0.169	0.363	CS2
28	P1Z-2	0.60	0.25	0.55	0.45	0.45	0.50	0.47	0.121	0.260	CS2
29	P1Z-3	0.65	0.40	0.50	0.70	0.45	0.50	0.50	0.117	0.219	CS2
30	P1Z-4	0.45	0.15	0.40	0.35	0.35	0.30	0.35	0.103	0.310	CS2
31	P1Z-5	0.20	0.20	0.15	0.30	0.70	0.25	0.23	0.202	0.675	CS1
32	P1Z-6	0.50	0.40	0.50	0.50	0.40	0.55	0.50	0.061	0.129	CS2
33	P1Z-7	0.50	0.35	0.45	0.60	0.55	0.45	0.47	0.088	0.181	CS2
34	P1Z-8	0.40	0.25	0.30	0.50	0.35	0.45	0.38	0.094	0.249	CS2

Table A1. *Cont.*

No.	Crack ID	Insp. 1	Insp. 2	Insp. 3	Insp. 4	Insp. 5	Insp. 6	Median	SD	CV	CS
35	P1Z-9	0.10	0.15	0.35	0.45	0.30	0.15	0.22	0.138	0.551	CS1
36	P1Z-10	0.10	0.15	0.30	0.25	0.30	0.10	0.20	0.095	0.474	CS1
37	P1Z-11	0.25	0.15	0.15	0.30	0.15	0.25	0.20	0.066	0.319	CS1
38	P1DZ-1	0.10	0.20	0.10	0.25	0.20	0.25	0.20	0.068	0.373	CS1
39	P1DZ-2	0.45	0.15	0.50	0.50	0.30	0.35	0.40	0.137	0.365	CS2

Table A2. Crack width measurements obtained with the proposed system for the same 39 cracks. Five measurements are acquired per crack from different standoff distances while imaging the same reference location on the crack. The table lists the individual measurements together with their mean, standard deviation (SD), and coefficient of variation (CV). All widths are in millimeters; CV is dimensionless. Condition states are those assigned from the manual median in Table A1.

No.	Crack ID	M 1	M 2	M 3	M 4	M 5	Mean	SD	CV	CS
1	P1DG1	0.85	0.87	0.81	0.82	0.86	0.84	0.026	0.031	CS1
2	P1DG2	0.47	0.48	0.50	0.42	0.62	0.50	0.074	0.149	CS1
3	P1DG3	0.62	0.60	0.54	0.50	0.44	0.54	0.073	0.136	CS2
4	P1DG4	0.85	0.98	0.91	0.84	0.86	0.89	0.058	0.065	CS2
5	P1DG5	0.62	0.83	0.76	0.85	0.72	0.76	0.092	0.122	CS2
6	P1DG6	1.10	1.19	1.20	1.23	1.26	1.20	0.060	0.050	CS3
7	P1I-1	1.45	1.52	1.38	1.23	1.44	1.40	0.109	0.078	CS3
8	P1I-2	0.72	0.74	0.75	0.76	0.85	0.76	0.050	0.066	CS2
9	P1I-3	0.65	0.64	0.71	0.95	0.63	0.72	0.134	0.188	CS2
10	P1I-4	0.45	0.50	0.52	0.40	0.60	0.49	0.075	0.153	CS2
11	P1I-5	0.93	0.93	0.91	0.93	0.94	0.93	0.011	0.012	CS2
12	P1I-6	1.72	1.94	2.01	2.05	2.09	1.96	0.146	0.075	CS3
13	P1I-7	0.72	0.73	0.52	0.68	0.70	0.67	0.086	0.128	CS2
14	P1I-8	0.41	0.42	0.42	0.55	0.48	0.46	0.059	0.130	CS1
15	P1I-9	0.43	0.45	0.46	0.49	0.49	0.46	0.026	0.056	CS1
16	P1I-10	0.55	0.61	0.62	0.64	0.65	0.61	0.039	0.064	CS2
17	P1I-11	0.43	0.44	0.46	0.47	0.47	0.45	0.018	0.040	CS1
18	P1I-12	0.44	0.50	0.50	0.50	0.50	0.49	0.027	0.055	CS1
19	P1I-13	0.40	0.42	0.43	0.41	0.42	0.42	0.011	0.027	CS1
20	P1I-14	0.50	0.51	0.52	0.54	0.85	0.58	0.149	0.256	CS2
21	P1I-15	0.41	0.43	0.48	0.49	0.51	0.46	0.042	0.091	CS1
22	P1I-16	0.40	0.44	0.50	0.48	0.75	0.51	0.137	0.267	CS1
23	P1I-17	0.41	0.43	0.42	0.50	0.51	0.45	0.047	0.104	CS2
24	P1I-18	0.41	0.42	0.35	0.45	0.41	0.41	0.036	0.089	CS2
25	P1I-19	0.42	0.45	0.35	0.40	0.43	0.41	0.038	0.093	CS2
26	P1I-20	0.48	0.50	0.49	0.35	0.50	0.46	0.064	0.139	CS1
27	P1Z-1	0.50	0.54	0.56	0.74	0.58	0.58	0.092	0.158	CS2
28	P1Z-2	0.63	0.64	0.71	0.64	0.65	0.65	0.032	0.049	CS2

Table A2. *Cont.*

No.	Crack ID	M 1	M 2	M 3	M 4	M 5	Mean	SD	CV	CS
29	P1Z-3	0.65	0.67	0.69	0.69	0.70	0.68	0.020	0.029	CS2
30	P1Z-4	0.47	0.49	0.47	0.81	0.47	0.54	0.150	0.277	CS2
31	P1Z-5	0.45	0.45	0.46	0.50	0.46	0.46	0.021	0.045	CS1
32	P1Z-6	0.55	0.54	0.60	0.59	0.58	0.57	0.026	0.045	CS2
33	P1Z-7	0.54	0.55	0.61	0.51	0.58	0.56	0.038	0.069	CS2
34	P1Z-8	0.41	0.43	0.44	0.43	0.42	0.43	0.011	0.027	CS2
35	P1Z-9	0.41	0.42	0.41	0.42	0.43	0.42	0.008	0.020	CS1
36	P1Z-10	0.43	0.48	0.49	0.37	0.47	0.45	0.049	0.110	CS1
37	P1Z-11	0.43	0.45	0.43	0.44	0.50	0.45	0.029	0.065	CS1
38	P1DZ-1	0.40	0.41	0.43	0.43	0.20	0.37	0.098	0.262	CS1
39	P1DZ-2	0.47	0.41	0.53	0.49	0.49	0.48	0.044	0.092	CS2

Table A3. Average measurement variability by condition state, computed from Tables A1 and A2. These values correspond to those reported in the main text.

Condition state	No. of Cracks	Manual SD (mm)	Manual CV	System SD (mm)	System CV
CS1 (Good)	15	0.078	0.357	0.046	0.099
CS2 (Fair)	21	0.124	0.269	0.062	0.106
CS3 (Poor)	3	0.394	0.220	0.105	0.068

Note: Condition states follow the AASHTO MBEI width thresholds for reinforced concrete elements: CS1 < 0.30 mm; CS2 0.30–1.27 mm; CS3 > 1.27 mm, assigned on the basis of the manual median.

References

1. Faris, N.; Zayed, T.; Fares, A. Review of Condition Rating and Deterioration Modeling Approaches for Concrete Bridges. *Buildings* **2025**, *15*, 219. [CrossRef]
2. Karakostas, C.; Quaranta, G.; Chatzi, E.; Zülfikar, A.C.; Çetindemir, O.; De Roeck, G.; Döhler, M.; Limongelli, M.P.; Lombaert, G.; Apaydın, N.M.; et al. Seismic Assessment of Bridges through Structural Health Monitoring: A State-of-the-Art Review. *Bull. Earthq. Eng.* **2024**, *22*, 1309–1357. [CrossRef] [PubMed]
3. Koch, C.; Georgieva, K.; Kasireddy, V.; Akinci, B.; Fieguth, P. A Review on Computer Vision Based Defect Detection and Condition Assessment of Concrete and Asphalt Civil Infrastructure. *Adv. Eng. Inform.* **2015**, *29*, 196–210. [CrossRef]
4. Poursaee, A.; Ross, B. The Role of Cracks in Chloride-Induced Corrosion of Carbon Steel in Concrete—Review. *Corros. Mater. Degrad.* **2022**, *3*, 258–269. [CrossRef]
5. AL-Ameeri, A.S.; Rafiq, M.I.; Tsioulou, O. Combined Impact of Carbonation and Crack Width on the Chloride Penetration and Corrosion Resistance of Concrete Structures. *Cem. Concr. Compos.* **2021**, *115*, 103819. [CrossRef]
6. Chen, W.; Hou, J.; Wang, Y.; Yu, M. Visualization Analysis of Concrete Crack Detection in Civil Engineering Infrastructure Based on Knowledge Graph. *Case Stud. Constr. Mater.* **2024**, *21*, e03711. [CrossRef]
7. AASHTO. *Manual for Bridge Element Inspection*, 2nd ed.; American Association of State Highway and Transportation Officials: Washington, DC, USA, 2019.
8. Spencer, B.F.; Hoskere, V.; Narazaki, Y. Advances in Computer Vision-Based Civil Infrastructure Inspection and Monitoring. *Engineering* **2019**, *5*, 199–222. [CrossRef]
9. Panigati, T.; Zini, M.; Striccoli, D.; Giordano, P.F.; Tonelli, D.; Limongelli, M.P.; Zonta, D. Drone-Based Bridge Inspections: Current Practices and Future Directions. *Autom. Constr.* **2025**, *173*, 106101. [CrossRef]
10. Dorafshan, S.; Maguire, M. Bridge Inspection: Human Performance, Unmanned Aerial Systems and Automation. *J. Civ. Struct. Health Monit.* **2018**, *8*, 443–476. [CrossRef]
11. Graybeal, B.A.; Phares, B.M.; Rolander, D.D.; Moore, M.; Washer, G. Visual Inspection of Highway Bridges. *J. Nondestruct. Eval.* **2002**, *21*, 67–83. [CrossRef]

12. Fayyad, T.M.; Taylor, S.; Feng, K.; Hui, F.K.P. A Scientometric Analysis of Drone-Based Structural Health Monitoring and New Technologies. *Adv. Struct. Eng.* **2025**, *28*, 122–144. [CrossRef]
13. Adibfar, A.; Razkenari, M.; Costin, A. Review and Assessment of Technical and Legal Challenges in Application of Unmanned Aerial Vehicles in Monitoring and Inspection of Bridges. *Intell. Transp. Infrastruct.* **2023**, *2*, liad023. [CrossRef]
14. Waqas, A.; Kang, D.; Cha, Y.-J. Deep Learning-Based Obstacle-Avoiding Autonomous UAVs with Fiducial Marker-Based Localization for Structural Health Monitoring. *Struct. Health Monit.* **2024**, *23*, 971–990. [CrossRef] [PubMed]
15. Villarino, A.; Valenzuela, H.; Antón, N.; Domínguez, M.; Cubillos, X.C.M. UAV Applications for Monitoring and Management of Civil Infrastructures. *Infrastructures* **2025**, *10*, 106. [CrossRef]
16. Morgenthal, G.; Hallermann, N.; Kersten, J.; Taraben, J.; Debus, P.; Helmrich, M.; Rodehorst, V. Framework for Automated UAS-Based Structural Condition Assessment of Bridges. *Autom. Constr.* **2019**, *97*, 77–95. [CrossRef]
17. Abdel-Qader, I.; Abudayyeh, O.; Kelly, M.E. Analysis of Edge-Detection Techniques for Crack Identification in Bridges. *J. Comput. Civ. Eng.* **2003**, *17*, 255–263. [CrossRef]
18. Hui, L.; Ibrahim, A.; Hindi, R. Computer Vision-Based Concrete Crack Identification Using MobileNetV2 Neural Network and Adaptive Thresholding. *Infrastructures* **2025**, *10*, 42. [CrossRef]
19. Gharehbaghi, V.; Farsangi, E.N.; Yang, T.Y.; Noori, M.; Kontoni, D.-P.N. A Novel Computer-Vision Approach Assisted by 2D-Wavelet Transform and Locality Sensitive Discriminant Analysis for Concrete Crack Detection. *Sensors* **2022**, *22*, 8986. [CrossRef] [PubMed]
20. Mohan, A.; Poobal, S. Crack Detection Using Image Processing: A Critical Review and Analysis. *Alex. Eng. J.* **2018**, *57*, 787–798. [CrossRef]
21. Cha, Y.-J.; Choi, W.; Büyüköztürk, O. Deep Learning-Based Crack Damage Detection Using Convolutional Neural Networks. *Comput.-Aided Civ. Infrastruct. Eng.* **2017**, *32*, 361–378. [CrossRef]
22. Chen, F.-C.; Jahanshahi, M.R. NB-CNN: Deep Learning-Based Crack Detection Using Convolutional Neural Network and Naïve Bayes Data Fusion. *IEEE Trans. Ind. Electron.* **2018**, *65*, 4392–4400. [CrossRef]
23. Li, Y.; Hu, W.; Dong, H.; Zhang, X. Building Damage Detection from Post-Event Aerial Imagery Using Single Shot Multibox Detector. *Appl. Sci.* **2019**, *9*, 1128. [CrossRef]
24. Cheng, J.C.P.; Wang, M. Automated Detection of Sewer Pipe Defects in Closed-Circuit Television Images Using Deep Learning Techniques. *Autom. Constr.* **2018**, *95*, 155–171. [CrossRef]
25. Mei, Q.; Gül, M.; Azim, M.R. Densely Connected Deep Neural Network Considering Connectivity of Pixels for Automatic Crack Detection. *Autom. Constr.* **2020**, *110*, 103018. [CrossRef]
26. Mei, Q.; Gül, M. A Cost Effective Solution for Pavement Crack Inspection Using Cameras and Deep Neural Networks. *Constr. Build. Mater.* **2020**, *256*, 119397. [CrossRef]
27. Mei, Q.; Gül, M. Multi-Level Feature Fusion in Densely Connected Deep-Learning Architecture and Depth-First Search for Crack Segmentation on Images Collected with Smartphones. *Struct. Health Monit.* **2020**, *19*, 1726–1744. [CrossRef]
28. Zuo, H.; Wang, T.; Mei, Q. Transformer-Based Automatic Tracking of Structural Crack Propagation. *Struct. Control Health Monit.* **2026**, *2026*, 2543110. [CrossRef]
29. Yang, X.; Li, H.; Yu, Y.; Luo, X.; Huang, T.; Yang, X. Automatic Pixel-Level Crack Detection and Measurement Using Fully Convolutional Network. *Comput.-Aided Civ. Infrastruct. Eng.* **2018**, *33*, 1090–1109. [CrossRef]
30. Liu, Y.; Yao, J.; Lu, X.; Xie, R.; Li, L. DeepCrack: A Deep Hierarchical Feature Learning Architecture for Crack Segmentation. *Neurocomputing* **2019**, *338*, 139–153. [CrossRef]
31. Manjunatha, P.; Masri, S.F.; Nakano, A.; Wellford, L.C. CrackDenseLinkNet: A Deep Convolutional Neural Network for Semantic Segmentation of Cracks on Concrete Surface Images. *Struct. Health Monit.* **2024**, *23*, 796–817. [CrossRef]
32. Liu, Y.-F.; Cho, S.; Spencer, B.F.; Fan, J.-S. Concrete Crack Assessment Using Digital Image Processing and 3D Scene Reconstruction. *J. Comput. Civ. Eng.* **2016**, *30*, 04014124. [CrossRef]
33. Peng, X.; Zhong, X.; Zhao, C.; Chen, A.; Zhang, T. A UAV-Based Machine Vision Method for Bridge Crack Recognition and Width Quantification through Hybrid Feature Learning. *Constr. Build. Mater.* **2021**, *299*, 123896. [CrossRef]
34. Kim, H.; Lee, J.; Ahn, E.; Cho, S.; Shin, M.; Sim, S.-H. Concrete Crack Identification Using a UAV Incorporating Hybrid Image Processing. *Sensors* **2017**, *17*, 2052. [CrossRef] [PubMed]
35. Zhang, J.; Chen, W.; Zhang, J. UAV-Based Quantitative Crack Measurement for Bridges Integrating Four-Point Laser Metric Calibration and Mamba Segmentation. *Autom. Constr.* **2026**, *182*, 106774. [CrossRef]
36. Hassouna, M.; Marzouk, M.; Fathalla, E. Automated Low-Cost Framework for Crack Measurements in RC Structures Using Deep Learning Approach. *Sci. Rep.* **2026**, *16*, 14678. [CrossRef] [PubMed]
37. Huamani, K.; Espinola-Diaz, L.; Bedriñana, L.A.; Málaga-Chuquitaype, C. Dual-Instance Automatic Segmentation and Damage Quantification of Concrete Spalling in RC Bridges. *Structures* **2026**, *88*, 111817. [CrossRef]
38. Jahanshahi, M.R.; Masri, S.F. A New Methodology for Non-Contact Accurate Crack Width Measurement through Photogrammetry for Automated Structural Safety Evaluation. *Smart Mater. Struct.* **2013**, *22*, 035019. [CrossRef]

39. Nyathi, M.A.; Bai, J.; Wilson, I.D. Concrete Crack Width Measurement Using a Laser Beam and Image Processing Algorithms. *Appl. Sci.* **2023**, *13*, 4981. [CrossRef]
40. Zhao, S.; Kang, F.; Li, J. Non-Contact Crack Visual Measurement System Combining Improved U-Net Algorithm and Canny Edge Detection Method with Laser Rangefinder and Camera. *Appl. Sci.* **2022**, *12*, 10651. [CrossRef]
41. Park, S.E.; Eem, S.-H.; Jeon, H. Concrete Crack Detection and Quantification Using Deep Learning and Structured Light. *Constr. Build. Mater.* **2020**, *252*, 119096. [CrossRef]
42. Huang, S.; Ding, W.; Huang, Y. An Accurate Image Measurement Method Based on a Laser-Based Virtual Scale. *Sensors* **2019**, *19*, 3955. [CrossRef] [PubMed]
43. Nyathi, M.A.; Bai, J.; Wilson, I.D. Deep Learning for Concrete Crack Detection and Measurement. *Metrology* **2024**, *4*, 66–81. [CrossRef]
44. Tse, K.-W.; Pi, R.; Sun, Y.; Wen, C.-Y.; Feng, Y. A Novel Real-Time Autonomous Crack Inspection System Based on Unmanned Aerial Vehicles. *Sensors* **2023**, *23*, 3418. [CrossRef] [PubMed]
45. Zuo, H.; Cespedes, R.; Zaldivar, Y.; Medina, D.; Fiestas, J.; Bedriñana, L.A.; Shirzad-Ghaleroudkhani, N.; Mei, Q. A UAV-Mounted Metrology System for Accurate Crack Measurement in Bridges. In Proceedings of the 13th International Conference on Bridge Maintenance, Safety and Management, Orlando, FL, USA, 6 July 2026.
46. Zaldivar, Y.; Zuo, H.; Shirzad-Ghaleroudkhani, N.; Mei, Q.; Fiestas, J.; Bedriñana, L.A. Integrating UAVs and Deep Learning for Automatic and Scalable Crack Detection and Quantification in Reinforced Concrete Bridges. *e-J. Nondestruct. Test.* **2026**, *31*. [CrossRef] [PubMed]